

STRESS CALCULATION IN WORM GEARS USING ELASTIC MULTIBODY MODELS

Christian Pfister^{1,2}, Jens Pfister¹, Lorin Kazaz² and Peter Eberhard²

¹Robert Bosch Automotive Steering GmbH, Richard Bullinger Str. 77, 73552 Schwäbisch Gmünd, Germany, {christian,jens}.pfister@bosch.com

²Institute of Engineering and Computational Mechanics, University of Stuttgart, Pfaffenwaldring 9, 70569 Stuttgart, Germany, {christian.pfister,lorin.kazaz,peter.eberhard}@itm.uni-stuttgart.de

ABSTRACT — Stresses in worm gears are calculated using elastic multibody models. Via model order reduction, systems of low order are deduced, which allow the consideration of long simulation periods with low calculation times. A general contact routine for the consideration of interactions between arbitrarily shaped surfaces is presented. Three examples are calculated with the presented methods and compared to reference finite element calculations. The focus of this comparison are occurring stresses in critical regions of the gear parts. The novel contribution of this work is the overall application of the presented methods on worm gears, to provide a fast and reliable way of stress determination in transient simulations.

1 Introduction

Electric power steering systems (EPS) nowadays are fully established in the area of modern passenger cars. Due to power-on-demand supply, they excel at a high energy efficiency compared to hydraulic systems. In addition, extra features like lane departure warnings, parking assistance and other autonomous driving functions are directly applicable with these systems.

In all EPS concepts, the steering support is generated by an electric drive, whose force is applied into the system by a servo gear unit, see [1]. Two common EPS concepts are the EPS *dual pinion* (EPSdp) and the EPS *column* (EPSc). They both use a worm drive to transmit a motor torque. In EPSc concepts this torque acts on the steering column directly. In EPSdp it powers a servo pinion which acts on the rack, see Figs. 1 and 2. The parts in such gear drives must meet defined load and durability specifications.

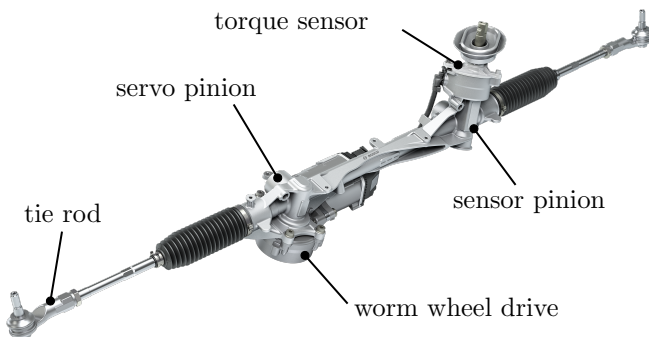


Fig. 1: EPSdp system with servo pinion [1]



Fig. 2: Worm wheel drive in the servo gear unit [1]

Common approaches for the dimensioning of worm gears rely on finite element analyses (FEA), which mainly cover just static load cases due to commonly high simulation times. The applied loads within these calculations are

determined in preceding multibody system (MBS) simulations. One drawback of this workflow is, that the deformations of the gear parts are initially neglected in the MBS simulations. Hence, the influence of the deformation on the system dynamics cannot be covered.

Usually, the material combinations of the worm and wheel rims are usually chosen to have low frictional coefficients. Typically, the wheel rim is made from elastomer material and the worm from steel, [2]. In this work material influences are neglected. Also frictional contact forces are omitted at this point.

The scope of this work is to present an elastic multibody system (EMBS) approach for transient simulations in worm wheel gears. By using model order reduction (MOR), calculation times can be lowered drastically. Furthermore, with the presented methods it is also possible to recover dynamic stresses for specific regions in a post-process.

The *floating frame of reference* approach (FFoR) is used to derive the governing equations of motion, see Section 2.1. This approach has already successfully been applied to spur gears [3], bevel gears and planetary gears [4]. All references have been calculated with the *Gear Train Module* (GTM), an EMBS tool-chain specialized on calculations of gears. Section 2.2 covers the stress recovery from reduced elastic bodies. In contrast to the already named applications, contact detection in worm gears requires a more general approach due their special geometry. Therefore, a special view is taken on a newly implemented contact routine in Section 2.3. In Section 3 some chosen calculation examples are shown. Finally, in Section 4, a conclusion about the results is given.

2 Elastic multibody systems with contact

Elastic multibody systems offer a good compromise between classic FEA and MBS methods. Among different existing EMBS concepts, the FFoR offers some very convenient features for the simulation of elastic gears, like linear model order reduction, leading to systems of small order. Another big advantage is the compatibility to classic multibody systems. Elastic bodies can easily be included into bigger MBS systems. Also, by omitting all elastic degrees of freedom, the equations of an elastic body reduce to those of a rigid body. This allows to find a good compromise between required precision and low calculation times.

2.1 Equations of motion

The elastic bodies used in this work are derived from full FE-models consisting of volume elements, see [5]. The equations of motion of a linear FE-body denotes

$$\mathbf{M}_f \cdot \ddot{\mathbf{q}}_f(t) + \mathbf{K}_f \cdot \mathbf{q}_f(t) = \mathbf{h}_f(t) \quad (1)$$

with the mass matrix \mathbf{M}_f , the stiffness matrix \mathbf{K}_f and the vector of elastic coordinates \mathbf{q}_f . The vector \mathbf{h}_f contains external forces acting on nodes, see [6].

2.1.1 Model order reduction by projection

A system of reduced order with dimension n_r can be gathered by projection of the full system of dimension n_f into a subspace. Using the projection \mathbf{V} matrix, by

$$\mathbf{q}_f \approx \mathbf{V} \cdot \mathbf{q}_r, \quad \text{where } n_r \ll n_f, \quad (2)$$

a reduced set of coordinates \mathbf{q}_r is defined. In this work, \mathbf{V} is assembled of global shape functions of the full FE-body by modal truncation. By solving Eq. (1)

$$(\mathbf{K}_f - \mathbf{M}_f \omega_i^2) \cdot \Phi_i = \mathbf{0} \quad (3)$$

for $i \in \{1, \dots, n_r\}$ eigenvalues ω_i , the corresponding system eigenmodes Φ_i are calculated. The reduced elastic coordinates are then calculated by

$$\mathbf{q}_f \approx \Phi_r \cdot \mathbf{q}_r \quad \text{with } \Phi_r = [\Phi_1, \Phi_2, \dots, \Phi_{n_r}]. \quad (4)$$

Inserting Eq. (4) into Eq. (1) and left multiplying with Φ_r^T leads to

$$\underbrace{\Phi_r^T \cdot \mathbf{M}_f \cdot \Phi_r}_{\mathbf{M}_r} \cdot \ddot{\mathbf{q}}_r(t) + \underbrace{\Phi_r^T \cdot \mathbf{K}_f \cdot \Phi_r}_{\mathbf{K}_r} \cdot \mathbf{q}_r(t) = \underbrace{\Phi_r^T \cdot \mathbf{h}_f(t)}_{\mathbf{h}_r} \quad (5)$$

with the reduced mass and stiffness matrices \mathbf{M}_r and \mathbf{K}_r and the generalized elastic forces \mathbf{h}_r . A corresponding damping matrix \mathbf{D}_r for consideration of material damping effects can be constructed as Rayleigh damping

$$\mathbf{D}_r = \alpha \mathbf{M}_r + \beta \mathbf{K}_r \quad (6)$$

with damping parameters α and β .

2.1.2 Floating frame of reference approach

The goal of the FFoR approach is to separate the overall movement of an elastic body into a rigid and a flexible part. A floating body reference frame (BRF) represents large nonlinear movements due to rigid body displacements and rotations with respect to a global frame. Linear elastic deformations are described relating to the BRF. The position vector $\rho(\mathbf{R}, t)$ of a material point P on an elastic body in the FFoR, see [5], can be written as

$$\rho(\mathbf{R}, t) = \mathbf{r}(t) + \mathbf{R} + \mathbf{u}(\mathbf{R}, t) \quad (7)$$

with the position vector $\mathbf{r}(t)$ of the BRF, the position \mathbf{R} of P with respect to the BRF in the undeformed configuration and the elastic deformation $\mathbf{u}(\mathbf{R}, t)$. Using reduced global shape functions $\Phi_r(\mathbf{R})$ from Eq. (4), elastic deformations can be written as

$$\mathbf{u}(\mathbf{R}, t) = \Phi_r(\mathbf{R}) \cdot \mathbf{q}_r(t). \quad (8)$$

The equations of motion for a free damped elastic body finally denotes

$$\underbrace{\begin{bmatrix} m\mathbf{I} & & \text{sym} \\ m\tilde{\mathbf{c}} & \mathbf{J} & \\ \mathbf{C}_l & \mathbf{C}_r & \mathbf{M}_r \end{bmatrix}}_{\mathbf{M}} \cdot \underbrace{\begin{bmatrix} \dot{\mathbf{v}} \\ \dot{\boldsymbol{\omega}} \\ \ddot{\mathbf{q}} \end{bmatrix}}_{\dot{\mathbf{z}}_{II}} = \underbrace{\begin{bmatrix} \mathbf{0} \\ \mathbf{0} \\ \mathbf{D}_r \cdot \dot{\mathbf{q}} + \mathbf{K}_r \cdot \mathbf{q} \end{bmatrix}}_{\mathbf{h}_e} + \mathbf{h}_g \quad (9)$$

wherein \mathbf{M} is the symmetric mass matrix containing the mass m , the inertia tensor \mathbf{J} , the center of mass \mathbf{c} and the coupling terms \mathbf{C}_l and \mathbf{C}_r . The vector of generalized coordinates $\dot{\mathbf{z}}_{II}$ holds the translational and rotational accelerations $\dot{\mathbf{v}}$, and $\dot{\boldsymbol{\omega}}$ of the rigid body motion and the elastic acceleration $\ddot{\mathbf{q}}$. In \mathbf{h}_e inner forces caused by elastic deformations are described. All other forces, including external single forces from contact interactions, see Section 2.3, are held in \mathbf{h}_g .

2.2 Stress recovery in reduced elastic bodies

According to the calculation of elastic deformations in Eq. (8), the concept of using global shape functions can also be applied to the calculation of the stress tensor, see [7]. Using the strain tensor

$$\epsilon_r(\mathbf{R}, t) = \mathbf{D}_{\epsilon u} \cdot \mathbf{u}(\mathbf{R}, t) \quad (10)$$

with $\mathbf{D}_{\epsilon u}$ describing the relation between displacement and strain, the stress of a reduced FE-body can be calculated by

$$\boldsymbol{\sigma}_r = \mathbf{H} \cdot \epsilon_r(\mathbf{R}, t) \quad (11)$$

with the constant material matrix \mathbf{H} . Using Eq. (4) with Eq. (10) and Eq. (11) yields the stresses of the reduced body

$$\boldsymbol{\sigma}_r = \underbrace{\mathbf{H} \cdot \mathbf{D}_{\epsilon u} \cdot \Phi_r(\mathbf{R})}_{\Psi_r} \cdot \mathbf{q}_r(t) \quad (12)$$

with shape functions of stress, the so-called stress modes Ψ_r . The quality of this stress approximation Ψ_r approach strongly depends on a good model order reduction quality.

2.3 Contact calculation in worm gears

A general spatial contact calculation in worm gears requires algorithms that cover the special geometry of such gear parts. The contact routine used in this work consists of two main parts, a coarse collision detection and a fine contact search.

2.3.1 Coarse collision detection

The coarse collision detection is covered by a general bounding volume hierarchy (BVH) scheme from [8]. The idea of this approach is to envelop a discrete geometry — like the surface of an finite element mesh — in geometrically simple bounding volumes that allow numerically cheap collision tests between themselves. To improve numerical efficiency, the bounding volumes are assembled in binary trees in a hierarchical manner. Two of such trees can then be traversed resulting in the colliding bounding volumes on leaf level. The bounding volumes that are used in this work are *discrete oriented polytopes* (k-DOPs), which can be seen as a generalization of *axis aligned bounding boxes* (AABBs), see [9].

Building BVH trees of k-DOPs A k-DOP is defined as a convex polytope, whose face normals are restricted to a small set of k fixed global orientations \mathbf{B} , see [10]. Further, for each chosen orientation there must exist an anti-parallel orientation. The tightest enveloping k-DOP of a set of points \mathbf{x} can be described by $\mathbf{d} \in \mathbb{R}^k$, where the relation

$$\mathbf{B}_i \cdot \mathbf{x} - d_i \leq 0, \quad i = \{1 \dots k\} \quad (13)$$

must be fulfilled. In fact, the k-DOP describes a minimum and maximum extend in a given orientation.

By recursive top-down calculation a binary tree of k-DOPs can automatically be constructed. Thereby, the root level k-DOP wraps the complete surface and a leaf level k-DOP contains just a single surface element. Figure 3 shows different levels of a BVH tree of a finite element worm gear mesh.

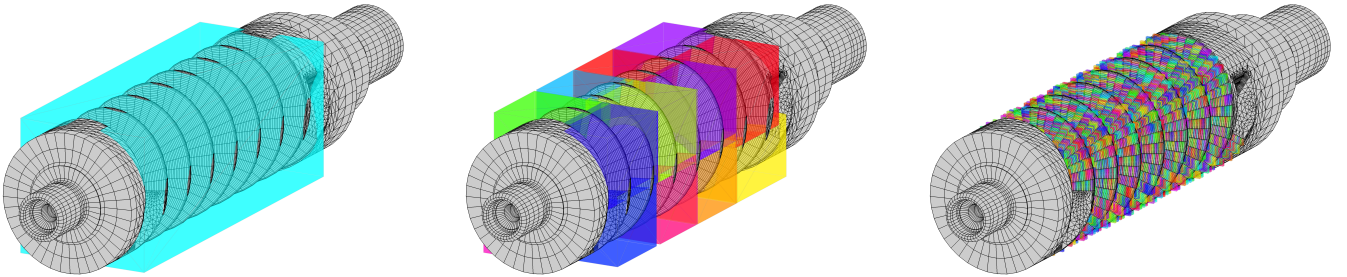


Fig. 3: Different BVH tree levels of an enveloped worm geometry; left: level 1, middle: level 5, right: level: 14/15 (leaf level)

Collision test between k-DOPs Due to the globally shared orientations \mathbf{B} , a collision test between two k-DOPs can be implemented as a simple interval test. Two k-DOPs dop1 and dop2 with corresponding extensions \mathbf{d}^1 and \mathbf{d}^2 are not overlapping if

$$\min(d_i^1) > \max(d_i^2) \quad || \quad \max(d_i^1) < \min(d_i^2) \quad \text{with } i = \{1, \dots, k/2\}, \quad (14)$$

where \min and \max denote the corresponding anti-parallel orientations on an interval i . Hence, two k-DOPs are overlapping, if they are intersecting at each tested interval. The set of colliding k-DOPs on leaf level for two intersecting BVH trees can be found by a recursive tree search. Different traversing algorithms are discussed in [9]. An exemplary result of a BVH tree search for the worm gear model that is used in this work is shown in Fig. 4. The BVH tree of the wheel envelops the potential contact surfaces on the tooth flanks.

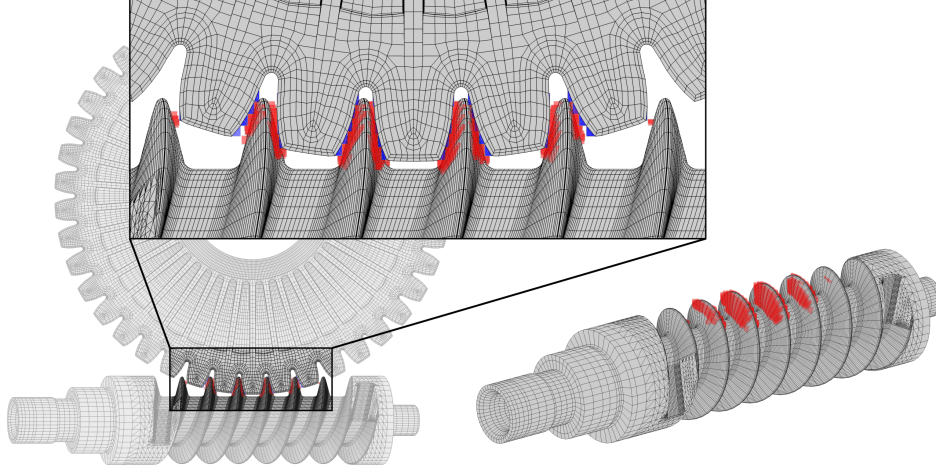


Fig. 4: Resulting k-DOPs of a binary tree search on the worm gear model; red: resulting k-DOPs of the worm, blue: resulting k-DOPs of the wheel

Alignment of k-DOPs While k-DOPs are invariant to translational movements of the underlying geometry, they must be realigned when the geometry performs rotary motions. A possible way of alignment can be done by a recalculation of the extensions \mathbf{d} from the hull points of the tumbled k-DOP. The result is a new aligned k-DOP, that envelops the original one.

Some remarks on using k-DOPs with deformable geometries Besides of rotational movements, k-DOPs also get invalid through deformations of the underlying geometry. Nevertheless, due to the extent of the bounding volumes, small deformations can usually be neglected.

For cases where this assumption is not valid, an update strategy proposed in [11] is used, that avoids a complete hierarchy recalculation. The leaves of a bounding volume hierarchy are recalculated according to the deformed mesh. Based on the recalculated leaf level k-DOPs, a parent of two related k-DOPs can easily be updated by the set union of the children \mathbf{d} values.

2.3.2 Fine contact search

For contact force determination, a general 3-D node to surface approach is used, see [3]. This routine works by a master-slave subdivision of two colliding bodies. The position vector \mathbf{x} on a quadrilateral surface element is expressible with natural coordinates ξ and η by the use of local shape functions

$$\mathbf{x}(\xi, \eta) = \frac{1}{4} \sum_{i=1}^4 (1 + \xi_i \xi)(1 + \eta_i \eta) \rho_i, \quad \xi_i, \eta_i \in [\pm 1] \quad (15)$$

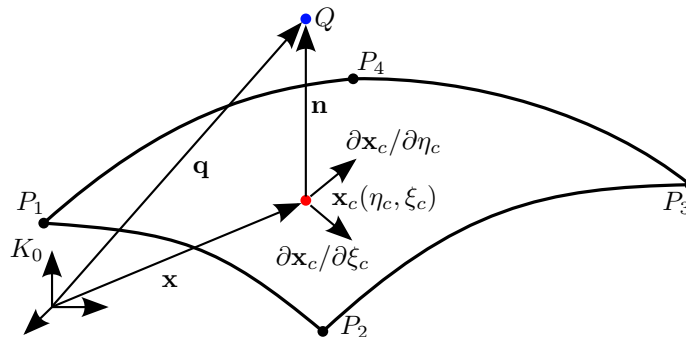


Fig. 5: Evaluation of a quadrilateral master-slave contact element

where ρ_i denotes the position vectors of the corner points P_i of an element. The projection \mathbf{x}_c of a slave node Q with its position vector \mathbf{q} on a quadrilateral master surface element, see Fig. 5, can be calculated by numerically solving

$$\frac{\partial \mathbf{x}}{\partial \xi} [\mathbf{q} - \mathbf{x}(\xi, \eta)] = 0, \quad \frac{\partial \mathbf{x}}{\partial \eta} [\mathbf{q} - \mathbf{x}(\xi, \eta)] = 0. \quad (16)$$

For a slave node that lies within the element borders, the penetration then becomes

$$g_n = \mathbf{n}(\mathbf{x}_c(\xi_c, \eta_c) - \mathbf{q}), \quad \text{with } \mathbf{n} = \frac{\partial \mathbf{x} / \partial \xi \times \partial \mathbf{x} / \partial \eta}{\|\partial \mathbf{x} / \partial \xi \times \partial \mathbf{x} / \partial \eta\|}. \quad (17)$$

For $g_n < 0$ penetration occurs. A penalty force acting on the slave node is then assembled by

$$\mathbf{f}_s = \mathbf{n} c_p |g_n| \quad (18)$$

with c_p denoting the penalty contact stiffness in normal direction. Due to the use of isoparametric elements, the force acting on the master element can be expressed by the forces $\mathbf{f}_{m,i}$ acting on the element nodes as

$$\mathbf{f}_{m,i} = -\frac{1}{4}(1 + \xi_i \xi_c)(1 + \eta_i \eta_c) \mathbf{f}_s. \quad (19)$$

The colliding k-DOPs from the coarse collision detection are the input to the fine contact search. The surface elements of the master k-DOPs are checked for contact with the corresponding surface nodes of the slave k-DOP.

3 Calculation examples

In this section some distinctive use cases of the presented methods are discussed and presented for three examples.

FE-model The investigated worm-wheel gear FE-model is shown in Fig. 6. It originates from an EPSdp steering system and consists of three separate bodies, worm, wheel body and wheel rim. For the scope of this work, the wheel body and the wheel rim are handled as one merged body called wheel. Some characteristic data of the FE-model are given in Tab. 1. Worm gear and wheel are modeled with an isotropic linear steel material.

EMBS preparation For the EMBS model, both bodies are reduced to a maximum number of 2000 elastic degrees of freedom. The eigenmodes are calculated for a restrained configuration. Figure 6 shows the restrained spots in blue color. This restriction matches with the mounting of the gears in the housing.

The BVH trees for the collision detection consider all possible contact surfaces. Therefore, any arbitrary flank pairing can potentially be calculated. This is mandatory for the calculation of multiple rotations in the gearing, see Section 3.2.2.

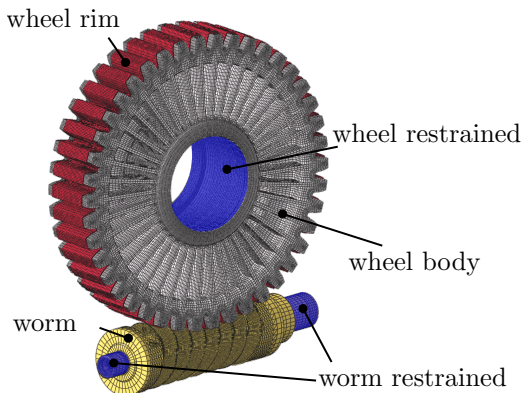


Fig. 6: Parts of the worm gear model

Tab. 1: Data of the worm gear model

category	parameter	worm	wheel
mesh	# nodes	90082	468587
	# elements	98666	406672
	# contact faces	10106	11760
material	Young's modulus	210 MPa	
	Poisson's ratio	0.3	
MOR	max. # modes	2000	

Reference FE-model The reference FE-model is built up equivalent to the EMBS. The restrained nodes are connected to a marker coinciding with the BRF in the EMBS approach via RBE2 coupling. These markers are used to restrict particular degrees of freedom or to induce external loads. In the FE-model, the gearing interactions are defined just in the immediate contact zone.

Example setups The calculation examples are an impact, a turn-in and a rolling contact simulation. An overview of all three configurations is shown in Fig. 7. In every case, a reference calculation is provided by an FE-simulation. In the impact scenario, the FE-reference is calculated by a dynamic FE-solving. For the turn-in and the rolling contact simulation, a quasi-static FE-reference is calculated as reference.

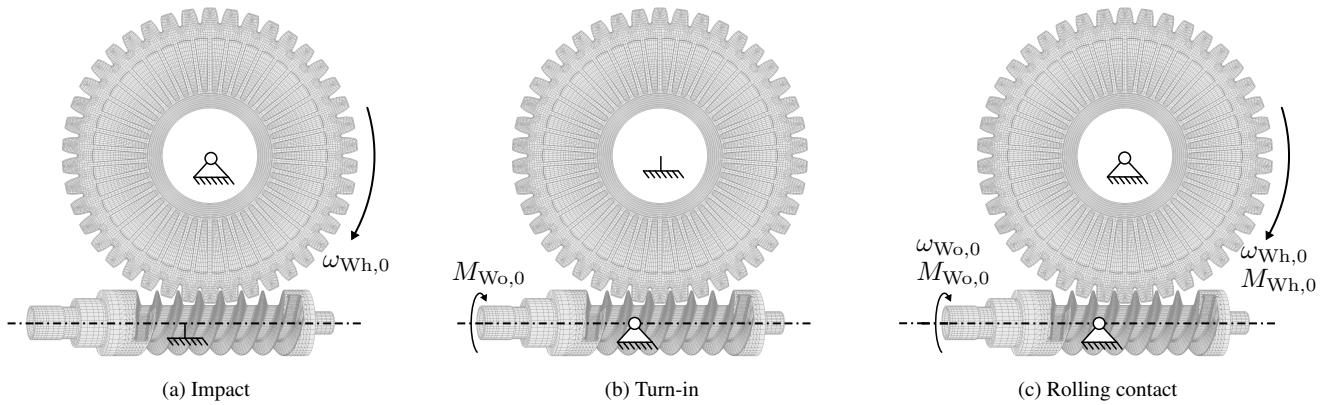


Fig. 7: Initial setup of the simulation examples

The nodes of stress evaluation are shown in Fig. 8. This includes regions with occurring tooth root stress and contact stress. Occurring stresses in these spots are of special interest for tooth root stress and pitting load capacity calculations, see [12].

All simulations are calculated on a workstation with an Intel Xeon E5-2643 CPU and 256 GB of main memory. To suppress speedups due to parallelization, which are different to interpret, only one of the CPU cores is used in every case.

3.1 Impact simulation

In the impact calculation, the worm is completely fixed in every rigid body degree of freedom. The wheel rotates about its axis of rotation, see Fig. 7a with a starting angular velocity of $\omega_{Wh,0}$. The duration of the impact is 0.5

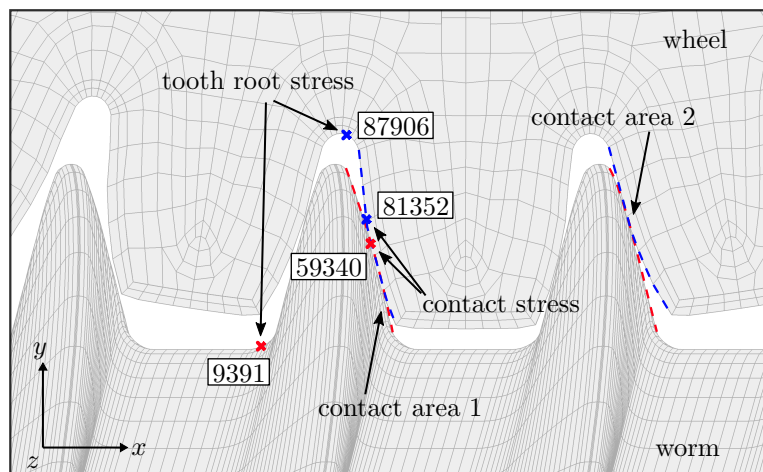


Fig. 8: Spots of stress evaluation at tooth roots and on tooth flanks

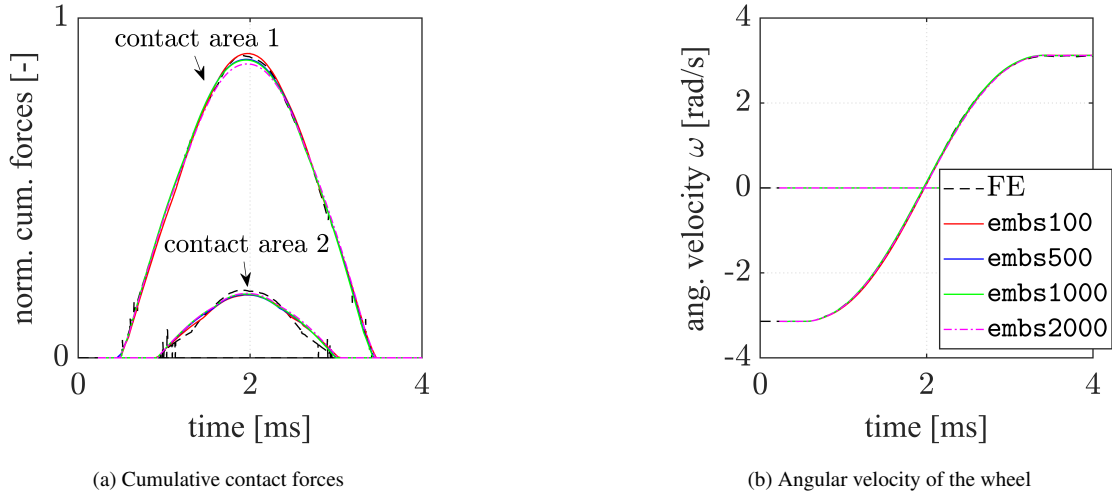


Fig. 9: Impact simulation for embs100, embs500, embs1000 and embs2000

ms, containing the full rebound phase. For the determination of the right number of eigenmodes to use, different configurations embs100, embs500, embs1000 and embs2000 with 100, 500, 1000 and 2000 elastic degrees of freedom per body, respectively are taken into account. The results obtained for the cumulative contact forces and kinematics are shown for all settings in Fig. 9. It can be seen, that already with embs100 the cumulative contact forces in both areas of contact can be approximated very well. This, subsequently, also leads to a high accordance in the angular velocity of the wheel, see Fig. 9b.

3.1.1 Tooth root stresses

The recovered tooth root stress components of the worm node 9391 are shown for every configuration in Fig. 10. Here, it can clearly be seen that the computed stress components for configuration embs100 and embs500 are inaccurate. The configurations embs1000 and embs2000 yield very good normal stresses σ_{xx} and σ_{yy} . This matches the effective direction of the acting contact forces. All other remaining stress components show insufficient (τ_{xy}) or wrong (σ_{zz} , τ_{xz} , τ_{yz}) stress results. This is in agreement with previous analyses for stress computations in gears, see [13].

The tooth root stress recovery of the wheel node 87906 turns out to be less accurate than on the worm, see Fig. 11. Even in embs2000, the normal stresses are very inaccurate. The reason for this attributes to the structural composition of the wheel. With its small teeth, the wheel turns out to be very stiff. Even using the first 2000 eigenmodes, there are only few modes, which describe the overall tooth deformation sufficiently, thus leading to poor stress recovery.

3.1.2 Contact stresses

As expected, the contact stresses in the performed EMBS calculations turn out to be inaccurate, for the worm gear node 59340, as well as for the wheel node 81352. The normal stresses σ_{xx} for both bodies are shown in Fig. 12. This is expected, since due to the modal truncation process, local deformations on the tooth flanks cannot be recovered very well in the extremely reduced models. However, these deformations are mandatory to get good accordance in the stress components. The investigation of stress in the tooth contact areas are therefore dismissed for the subsequent work.

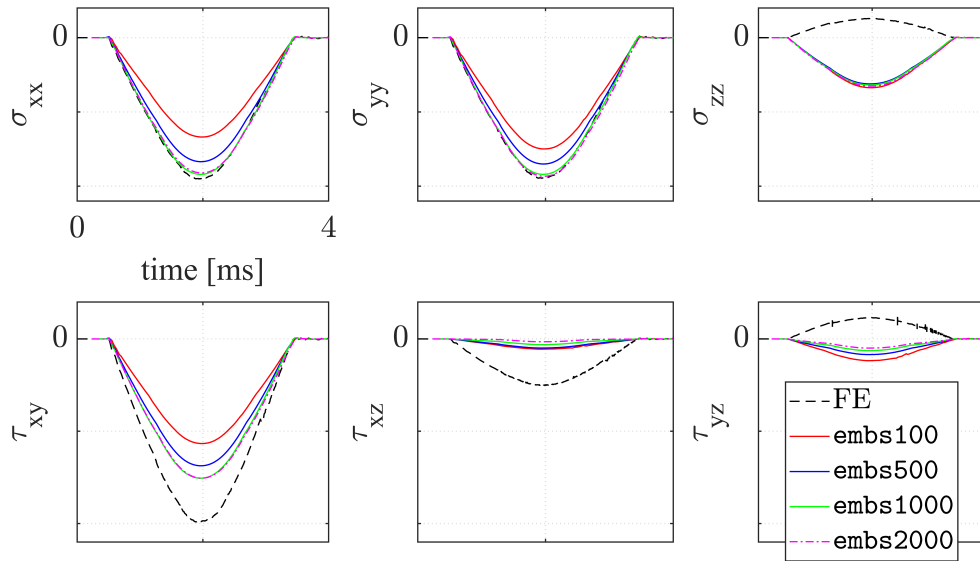


Fig. 10: Recovered normalized stress tensor components of worm node 9391

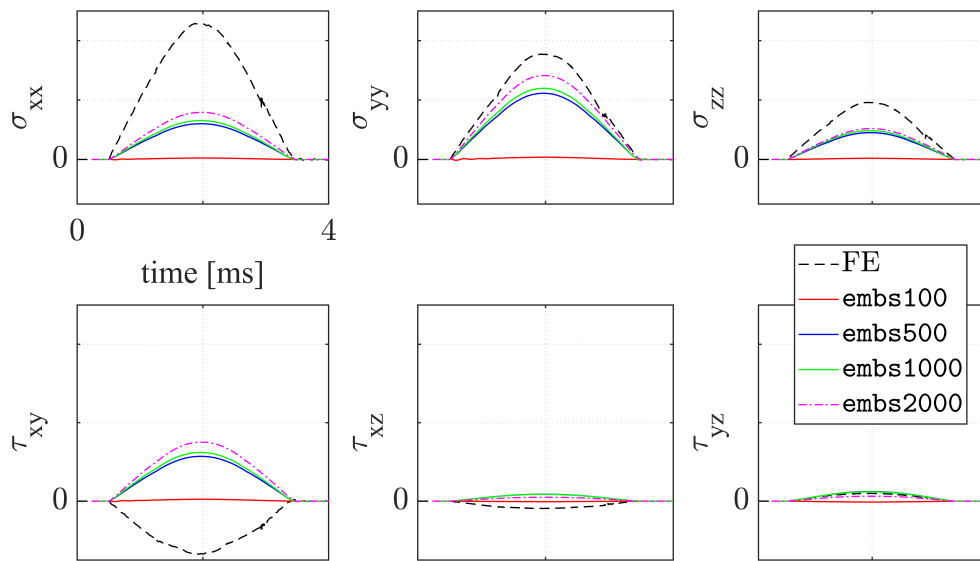


Fig. 11: Recovered normalized stress tensor components of wheel node 87906

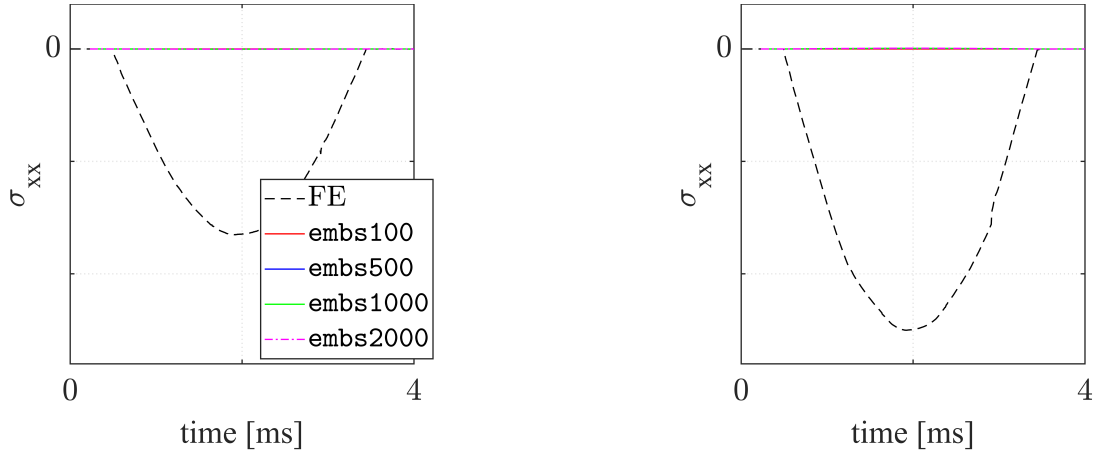


Fig. 12: Recovered normalized normal stress for worm node 59340 (left) and wheel node 81352 (right)

3.1.3 Simulation time

A great feature of EMBS are fast simulation times due to compact models. An overview of the calculation duration for all calculated configurations is given in Tab. 2. Preprocessing time mainly contains the duration of the one-time execution of the eigenanalysis for both bodies that is needed to generate the elastic bodies for the EMBS simulations.

Regarding time integration, a significant advantage of the EMBS can be seen. Even the embs2000 configuration is roughly 51 times faster than the FE-calculation.

Tab. 2: Time comparison for the impact simulation in seconds

	preprocessing	time integration
FE	-	≈ 71000
embs100		17
embs500		70
embs1000	23094	339
embs2000		1374

3.2 Quasi-static simulations

For the quasi-static simulations, a steady-state is calculated on EMBS side. The obtained steady-state is then used as an input for static FE-analyses.

3.2.1 Turn-in

In this simulation setup, the torque driven ($M_{W_0,0}$) worm gear turns into the fixed wheel until both bodies fully come to rest in an equilibrium state, see Fig. 7b. Based on the last section, the embs1000 configuration is used. A fast decay of elastic vibrations due to the initial impact results from material damping parameters. In the final state, the torque acting on the worm gear is balanced by the contact forces.

The relative stress deviations between the FE-reference and embs1000 in the equilibrium state are shown in Tab. 3. As in the impact simulation, stress recovery on the worm gear delivers clearly better results than on the wheel. A qualitative comparison of the von Mises stress between the FE-simulation and the EMBS simulation on the worm gear is shown in Fig. 13. Again, the pattern of the occurring tooth root stress yields very similar results with both methods and the contact stress is determined poorly in the EMBS simulation.

Tab. 3: Relative deviation of stress components and equivalent stress in equilibrium state

node	stress deviation (%)							von Mises	Rankine
	σ_{xx}	σ_{yy}	σ_{zz}	τ_{xy}	τ_{xz}	τ_{yz}			
9391	9.32	4.59	31.42	9.17	105.90	122.49	10.51	2.77	
87906	59.04	212.54	505.97	45.78	84.62	251.80	48.18	22.46	

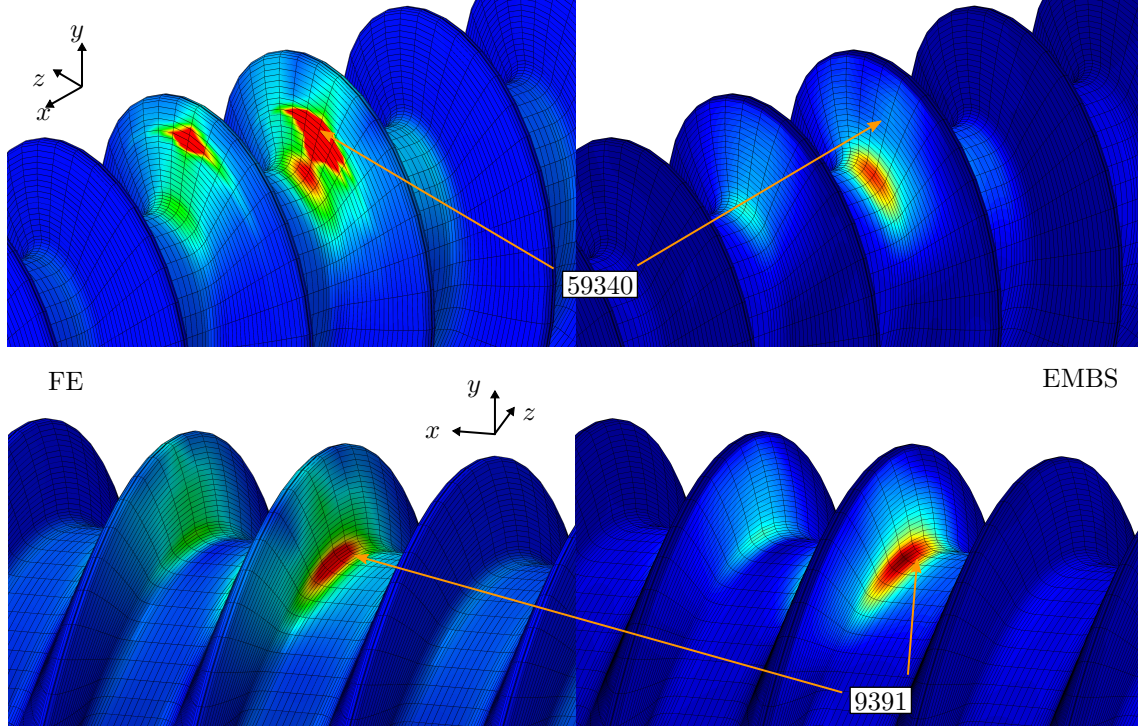


Fig. 13: Comparison of qualitative von Mises stress distribution between FE (left) and EMBS (right) on the worm gear at equilibrium

3.2.2 Rolling contact

The last example is a quasi-static roll off simulation. The initial configuration for this simulation is shown in Fig. 7c. The worm gear is driven with a constant torque $M_{W_0,0}$ and has a starting velocity of $\omega_{W_0,0}$. According to the gear transmission ratio, the wheel is loaded with a breaking torque $M_{Wh,0}$ and an appropriate starting velocity $\omega_{Wh,0}$. The simulation results are shown in Fig. 14. After an initial impact at the beginning, with high resultant amplitudes, a steady-state of motion is reached very fast. An intermediate state at 50 ms is used as an input for a static FE-calculation. In this state the worm gear has completed one rotation, so node 9391 is still in the area of critical stress. The relative stress deviations between the FE-reference and embs1000 are shown in Tab. 4. Similar to the previous simulations, σ_{xx} and σ_{yy} agree well, whereas large deviations can be noticed especially in the shear stresses.

Tab. 4: Relative deviation of stress components and equivalent stress in steady-state

node	stress deviation (%)						von Mises	Rankine
	σ_{xx}	σ_{yy}	σ_{zz}	τ_{xy}	τ_{xz}	τ_{yz}		
9391	1.49	2.36	27.71	15.76	116.91	133.27	16.67	9.28

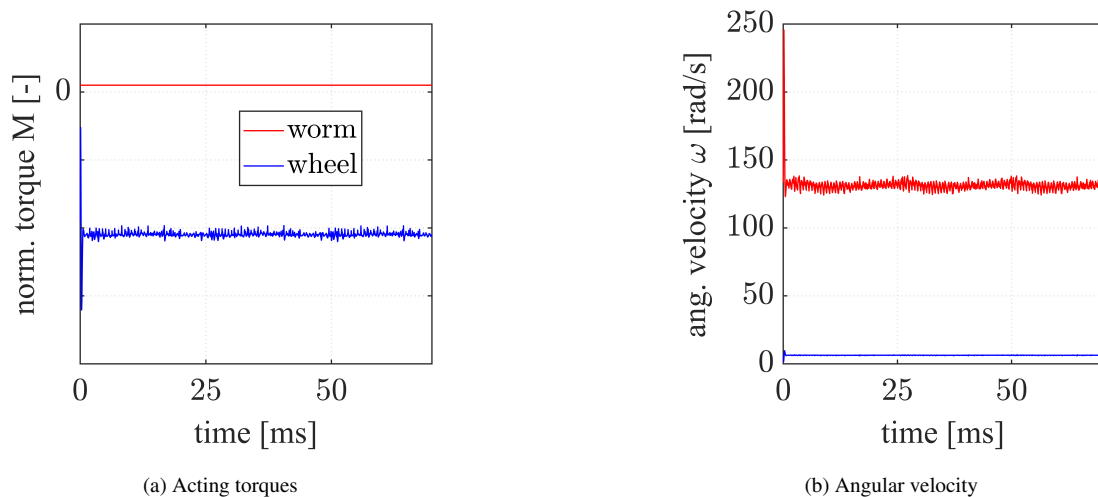


Fig. 14: Rolling contact simulation for embs1000

4 Conclusions

The simulations in this work show manifold results, regarding the accuracy of recovered stress. Tooth root stresses on the worm can be calculated accurately for the most affected components of the stress tensor. In contrast, stresses calculated for the wheel are more inaccurate in every tested configuration. The possible reason for this is the poor approximation of the tooth bending in the modal basis. Similar counts for the contact stresses on both bodies, where the deformation on the tooth flanks is approximated insufficiently. Beside of taking more eigenmodes into account, this could be improved, by using more advanced model order reduction techniques, as reported in [13].

Anyway, the approach allows a rough estimation of stress values in tooth root, with fast calculation times. A good approximation of the overall motion could be used as starting a point for a succeeding static FE-analyses.

To improve the investigated model of this work in a practical way, more effort has to be put into the inclusion of different material models, to consider the characteristics of the elastomer material of the wheel rim. Also, frictional contacts must be included to get a more precise prediction of the overall motion of the worm gear.

References

- [1] P. Pfeffer and M. Harrer, *Steering Handbook*. Heidelberg: Springer International Publishing, 2017.
- [2] B. Schlecht, *Maschinenelemente 2 (in German)*. Ing. Maschinenbau, Pearson Studium, 2010.
- [3] P. Ziegler, *Dynamische Simulation von Zahnradkontakten mit elastischen Modellen (in German)*. Dissertation, Schriften aus dem Institut für Technische und Numerische Mechanik der Universität Stuttgart, Band 23, Aachen: Shaker Verlag, 2012.
- [4] T. Do, *Dynamics Simulation of Elastic Gears with Different Flank Profiles*. Dissertation, Schriften aus dem Institut für Technische und Numerische Mechanik der Universität Stuttgart, Band 35, Aachen: Shaker Verlag, 2015.
- [5] R. Schwertassek and O. Wallrapp, *Dynamik flexibler Mehrkörpersysteme: Methoden der Mechanik zum rechnergestützten Entwurf und zur Analyse mechatronischer Systeme (in German)*. Grundlagen und Fortschritte der Ingenieurwissenschaften, Braunschweig: Vieweg+Teubner Verlag, 2014.
- [6] K. Bathe, *Finite Element Procedures*. Upper Saddle River: Prentice Hall, 1996.
- [7] C. Tobias, *Schädigungsberechnung in elastischen Mehrkörpersystemen (in German)*. Dissertation, Schriften aus dem Institut für Technische und Numerische Mechanik der Universität Stuttgart, Band 24, Aachen: Shaker Verlag, 2012.
- [8] G. Zachmann, “Rapid collision detection by dynamically aligned dop-trees,” in *Proceedings of the IEEE Virtual Reality Annual International Symposium*, (Atlanta), pp. 90 – 97, 1998.
- [9] C. Ericson, *Real-Time Collision Detection*. Boca Raton: CRC Press, 2004.

- [10] Klosowski, James T. and Held, Martin and Mitchell, Joseph S. B. and Sowizral, Henry and Zikan, Karel, "Efficient collision detection using bounding volume hierarchies of k-dops," *IEEE Transactions on Visualization and Computer Graphics*, vol. 4, no. 1, pp. 21–36, 1998.
- [11] G. van den Bergen, "Efficient collision detection of complex deformable models using aabb trees," *Journal of Graphics Tools*, vol. 2, no. 4, pp. 1–13, 1998.
- [12] DIN 3996, *Tragfähigkeitsberechnung von Zylinder-Schneckengetrieben mit Achswinkel $\Sigma = 90^\circ$ (in German)*. Berlin: Beuth Verlag, 1996.
- [13] D. Schurr, P. Holzwarth, and P. Eberhard, "Investigation of dynamic stress recovery in elastic gear simulations using different reduction techniques," *Computational Mechanics*, pp. 1–18, 2017.